

THE HANLE EFFECT AS A DIAGNOSTIC OF MAGNETIC FIELDS IN STELLAR ENVELOPES. II. SOME THEORETICAL RESULTS FOR RESOLVED LINE PROFILES

R. IGNACE,^{1,2} J. P. CASSINELLI,¹ AND K. H. NORDSIECK¹

Received 1998 September 8; accepted 1999 February 27

ABSTRACT

A magnetic field diagnostic of stellar winds that uses the Hanle effect is discussed. This diagnostic pertains to the modification of resonance-line-scattering polarization in the presence of magnetic fields. The case for resolved polarized profiles of optically thin emission lines is considered, and some analytic results for an expanding equatorial disk are derived. Numerical results for a dipole magnetic field embedded in a spherical outflow are also presented. Although the considerations are somewhat simplified, the primary conclusion is that the modification or creation of line profile polarization by the Hanle effect can be used to discriminate between different magnetic field geometries and to estimate the magnetic field strength in the region of line formation.

Subject headings: line: formation — polarization — scattering — stars: atmospheres — stars: magnetic fields

1. INTRODUCTION

The scattering of radiation by resonance lines will in general lead to linearly polarized light, even in the absence of a magnetic field (e.g., Hamilton 1947), and an analysis of the resulting spectropolarimetric line profile provides information on the distribution of scatterers (e.g., Poeckert & Marlborough 1978; McLean 1979; Wood, Brown, & Fox 1993; Wood & Brown 1994; Ignace 1998a, 1998b). In the presence of a magnetic field, the well-known Zeeman effect can alter dramatically both the intensity and the polarization of the line emission. However, in most astrophysical applications, measurements based on the Zeeman effect are hampered by various line-broadening processes, such as thermal, rotational, and wind broadening. These lead to significant polarimetric cancellation unless the field is quite strong, with kilogauss strengths, as, for example, the peculiar A and B stars (Babcock 1958; Borra & Landstreet 1980; Shore & Brown 1990; Shore et al. 1990; Mathys 1991). However, a lesser known atomic process called the “Hanle effect” leads to a modification of the *linear* polarization arising from resonance-line scattering, in contrast to the circular polarization associated with the Zeeman effect. Moreover, the Hanle effect has sensitivities to magnetic fields in the subkilogauss regime.

The discovery of the Hanle effect dates back to the early part of the twentieth century, when Hanle (1924; after whom the effect was eventually named) and Eldridge (1924) found that the change in the linear polarization of resonance-scattered radiation in the presence of a magnetic field was related to the *radiative lifetime* of the atomic transition. Atomic physicists have used the Hanle effect to derive transition probabilities by observing the response of the polarimetric signal to a known ramped magnetic field. For astrophysical applications the transition probabilities are taken as given, and here we explore the possibilities of employing the Hanle effect to derive the properties of stellar magnetic fields.

A general discussion of the Hanle effect in various physical contexts can be found in Moruzzi & Strumia (1991). For astrophysical applications the Hanle effect has thus far been used only in studies of the Sun, for which a summary of recent theoretical and observational results can be found in the proceedings on solar polarization presented in Stenflo & Nagendra (1996). A major difference between applications to the Sun as compared with distant stars is that the specific intensity of light can be observed from the Sun, but only the integrated flux of light is observed from distant stars. Even in cases where there is some spatial resolution of a star (e.g., Betelgeuse, as reported by Gilliland & Dupree 1996), the resolved portions comprise a major fraction of the total stellar surface, because the spatial resolution is many orders of magnitude below that of solar observations. Consequently, the primary value of the Hanle effect will be as a diagnostic tool of global stellar magnetic fields.

In a previous paper, Ignace, Nordsieck, & Cassinelli (1997, hereafter INC) investigated consequences of the Hanle effect on the total flux of line emission from an optically thin circumstellar envelope. One of the most exciting aspects of the Hanle effect is that not only is the line polarization modified at each frequency, but a net change in the profile-integrated polarization is also produced. Thus, the Hanle effect provides a useful magnetic diagnostic even for rather low-resolution spectropolarimetric observations. INC showed that the total line polarization from an ensemble of line measurements can be used to infer both the magnitude and the topology of the circumstellar magnetic field. Moreover, the cross section of resonance-line scattering can exceed that of Thomson scattering by free electrons by orders of magnitude; hence resonance-line polarization can occur in a broader class of stellar envelopes than will continuum polarization from electron scattering. Here we extend previous work by considering the additional information available in resolved polarized profiles of optically thin lines.

Expanding winds provide a particularly useful framework for our study, because the presence of a bulk flow produces a high degree of line broadening, with full widths of about 2000–4000 km s⁻¹ for typical hot star winds. The expansion also leads to a simplification of the radiation transfer, based on the Sobolev escape probability method

¹ Department of Astronomy, University of Wisconsin, 5534 Sterling Hall, 475 North Charter Street, Madison, WI 53706-1582.

² Presently at Department of Physics and Astronomy, Kelvin Building, University of Glasgow, Glasgow G12 8QQ, Scotland, UK; rico@astro.gla.ac.uk

(Sobolev 1957, 1960). For winds where the radial velocity greatly exceeds the thermal Doppler broadening, Sobolev theory predicts that the flux of line emission at frequency ν emerges from a narrow zone near its corresponding isovelocity surface. An isovelocity surface is defined to be the locus of points for which the projected flow velocity is constant along different lines of sight through the envelope (Mihalas 1978).

Winds lead to simplifications of the radiation transfer, and they interact in interesting ways with stellar magnetic fields. If the field is weak, an energetic and spherical wind can draw out the field into a nearly radial distribution, with several sectors of oppositely directed magnetic field. If the star is rotating, the field can be drawn out into a spiral pattern (Parker 1958; Brandt 1970), with the field following streak lines in the stellar wind (Ignace, Cassinelli, & Bjorkman 1998). A field that is sufficiently strong can drive the outflow by way of the magnetic rotator wind mechanism (Friend & MacGregor 1984; Poe & Friend 1986; Cassinelli 1998). Finally, the presence of a field can produce non-thermal emissions (Chen & White 1991) and particle acceleration (Biermann & Cassinelli 1993). There is a real need for diagnostic tools to derive the magnitude and configuration of magnetic fields in the subkilogauss range, since the practical detection of stellar magnetic fields using the Zeeman effect typically requires field strengths around 1000 G or more (although see Carter et al. 1996 and Donati et al. 1997).

In § 2 we introduce the aspects of the Hanle effect that are needed for our study of polarized line profiles. In § 3 attention is focused on the optically thin case, and analytic expressions are derived for two simplified magnetic geometries: an axial and toroidal field. For both of these cases, results are presented for an equatorial disk wind. A numerical simulation of a dipole magnetic field in a spherical flow is also given. Concluding remarks are presented in § 4. Finally, an Appendix details the analytic case of a toroidal field in a disk.

2. THE HANLE EFFECT IN EXPANDING WINDS

2.1. *The Theory of the Hanle Effect*

A description of the Hanle effect was given in INC (and references therein). Here we summarize a few of the essential features of the theory. The consequences of the Hanle effect for resonance-line-scattering polarization can be explained in terms of the classical damped oscillator model for the scattering of radiation by a bound electron. In the classical model, the absorption of light will induce oscillations of the atom in two orthogonal directions. The basic physics of the Hanle effect is that the components of the electron motion that are transverse to the magnetic field will be made to precess, owing to the $\mathbf{v} \times \mathbf{B}$ Lorentz force on the electron. If there were no magnetic field present, the atomic oscillator would emit radiation at a fixed position angle, but with a magnetic field, the atom is caused to emit at a sequence of position angles. We refer to this precessional motion of the electron as “Hanle precession.”

For a free electron, the distribution of scattered light is a superposition of two orthogonal dipole oscillators. However, scattering by a resonance line differs from a free electron in that the scattering is partly dipolar (like a free electron) but also partly isotropic. For resonance lines the relative contributions depend on the j quantum number of

the lower level and the Δj of the transition (Chandrasekhar 1960). In the notation of Chandrasekhar, E_1 represents the fraction of the scattering that is dipolar, and $1 - E_1$ is the fraction that is isotropic.

For simplicity let us consider an atom that scatters purely dipole radiation, for which $E_1 = 1$. Furthermore, the incident light is completely unpolarized. Referring to Figure 1, we illustrate how the Hanle effect can alter the polarization by considering two viewing perspectives of a scattering event. The unpolarized beam has intensities $I_x = I_y$ and is incident to the scattering atom from the left, as shown. For case *a*, an observer is positioned to see the line radiation as scattered through a right angle. In the absence of a magnetic field, the scattered light is 100% polarized. If a magnetic field is oriented along the line of sight, then the y -component of the atomic oscillator that scatters light toward the observer precesses about the magnetic field, whereas the x -component parallel to the field remains fixed. Thus, relative to the unchanged intensity I_x , the component I_y is reduced, and a new component I_z is produced; hence the Hanle precession results in a net depolarization.

In contrast, an observer situated to see forward scattering, as in case *b* of Figure 1, would measure zero polarization in the absence of a field. But with a magnetic field, a net polarization is observed that is oriented along the direction of the magnetic field. So, we see that the Hanle effect can create or destroy polarization depending on the magnetic and scattering geometries. This simple pictorial representation for a single scatterer is useful for interpreting the polarization that results in more complicated geometries.

The primary parameter governing the degree to which the Hanle precession will be important is the ratio of the Larmor frequency, ω_{Lar} , to the radiative frequency, A_{ul} , of the line transition (with upper and lower levels u and l). The Larmor frequency is the oscillator’s precession rate; the radiative frequency is its radiative rate. In the Hanle phase function for the transfer of polarized light (see Appendix A of INC), the ratio $\omega_{\text{Lar}}/A_{ul}$ appears in the angular parameter α_2 , defined by

$$\tan \alpha_2 = \frac{2g_{\text{Lan}} \omega_{\text{Lar}}}{A_{ul}} = \frac{B}{B_{\text{Hanle}}}, \quad (1)$$

where g_{Lan} is the Landé factor, B is in units of Gauss, and B_{Hanle} is the Hanle field sensitivity, defined as

$$B_{\text{Hanle}} = 56.9 \frac{A_9}{g_{\text{Lan}}} \text{ G}, \quad (2)$$

with A_9 the Einstein transition probability normalized to 10^9 s^{-1} . The Hanle diagnostic is most sensitive to the magnetic field strength at which $\tan \alpha_2$ is on the order of 1; hence $B \approx B_{\text{Hanle}}$. If the ratio $\omega_{\text{Lar}}/A_{ul}$ is large, the Hanle precession becomes complete, and increasing the field strength yields little change in the observed polarization. In this situation the Hanle effect is said to be “saturated.” We will return to the importance of the ratio $\omega_{\text{Lar}}/A_{ul}$ and saturation in discussions of various cases presented in § 3. Naturally, if the ratio is small, the line polarization is little altered by the field. The important result here is that for a given magnetic field, lines of different A -values will yield different polarimetric signals in a predictable way; hence multiline observations can be used to infer the full vector magnetic field (i.e., both its magnitude and its direction). It is conve-

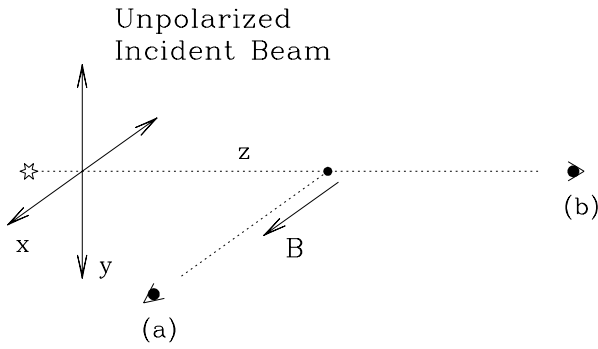


FIG. 1.—Simple example to illustrate the Hanle effect. Case *a*: a beam of light that is unpolarized scatters through a right angle. If $B = 0$, the polarization is 100%, but the presence of a magnetic field results in a net depolarization. Case *b*: the forward scattered beam remains unpolarized in the case of $B = 0$, but with a field transverse to the scattering direction, a net polarization results. Hence, the Hanle effect can either increase or decrease the polarization depending on the scattering and viewing geometry.

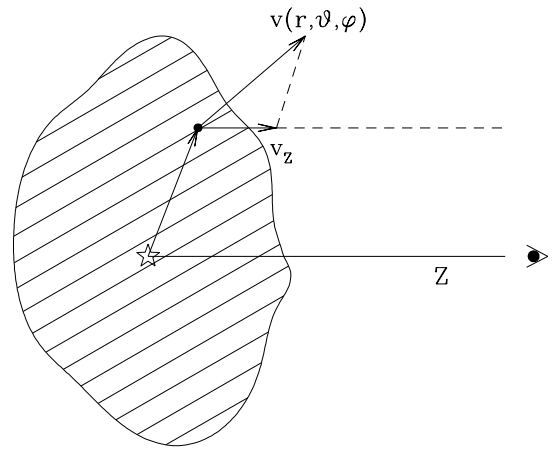


FIG. 2.—Doppler shift v_z that results from the bulk motion of a circumstellar flow. The Z -axis is taken to be the line of sight between the observer and the star. The observed velocity shift v_z is the projection of the vector velocity onto the line of sight.

nient here to introduce the shorthand $k_B = B_*/B_{\text{Hanle}}$ that will be used to relate the Hanle effect in the model line profile calculations to the surface magnetic field of the star, B_* . So, for $k_B = 0$, there is no Hanle effect, and $k_B \gg 1$ corresponds to the saturated limit.

2.2. The Theory of Line Formation in Stellar Winds

A P Cygni line profile is composed of four primary components: (1) a photospheric line contribution, (2) emission from material in the wind, (3) absorption of the stellar continuum by the intervening wind on the near side of the star, and (4) occultation of the wind emission produced at the far side of the star. These components combine to produce a typical P Cygni line that has shortward-shifted (to be referred to as “blueshifted”) absorption and longward-shifted (to be referred to as “redshifted”) emission. For simplicity of calculation, we employ Sobolev theory to compute the polarized line profiles. The line opacity is approximated as a δ function in frequency; hence the emission and absorption at each frequency in the wind-broadened line is formed in an isovelocity zone with constant Doppler shift Δv_z from line center, where Z is the coordinate along the observer’s line of sight (see Fig. 2).

There are two basic steps to the calculation of line profiles using the Sobolev formalism: identify the isovelocity zones and compute the line transfer through each zone. The locus of points making up a given isovelocity zone is derived from

$$\Delta v_z = -v_{\text{ul}} \frac{v_z}{c} = -\frac{v_z}{\lambda_{\text{ul}}}, \tag{3}$$

where v_z is the line of sight velocity shift given by

$$v_z = -\mathbf{v} \cdot \hat{Z}. \tag{4}$$

The velocity field is in general $\mathbf{v} = v(r, \vartheta, \varphi)$, with (r, ϑ, φ) being spherical coordinates of the star system. Note that in Figure 3, the velocity vector as drawn is not in the plane of the figure.

To represent the line radiation field, the Stokes 4-vector \mathbf{I}_v formalism is used, with Stokes parameters $I_v, Q_v, U_v,$ and V_v (Chandrasekhar 1960; Collins 1989). Since only the isovelocity zone at constant v_z contributes to the flux at the

corresponding frequency in the line, the observed scattered radiation is

$$\mathcal{F}_{v,s} = \frac{1}{d^2} \int_{v_z} I_v dA, \tag{5}$$

where dA is a differential area element perpendicular to the line of sight and d is the distance to the star. Neglecting both the stellar occultation and the intervening wind absorption of the stellar continuum, the intensity of scattered light is

$$I_v = \int_0^{\tau_{\text{sob}}} S_v e^{-\tau} d\tau, \tag{6}$$

where S_v is the Stokes source function and τ_{sob} is the Sobolev optical depth. In a wind where the line formation arises purely from resonance-line scattering (i.e., no col-

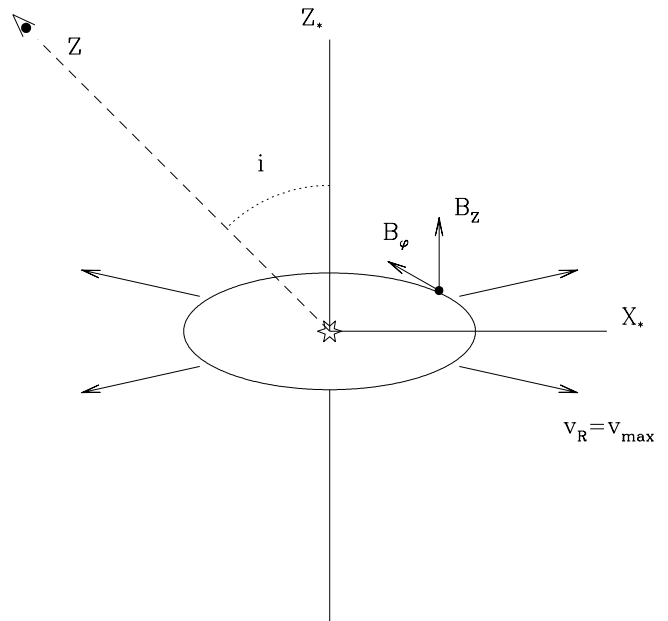


FIG. 3.—Planar equatorial disk geometry. An observer located toward the upper left views a star with a radially expanding disk at an inclination i from the symmetry axis. The X_* -axis is shown to lie in the Z_* - Z plane. A point in the disk has cylindrical coordinates $(R, \varphi, 0)$.

lisional deexcitation or continuous emission by the wind), the source function is determined by

$$S_v = \frac{1}{4\pi} \int_{4\pi} [1 - \beta_d(\hat{n}_i)] \mathcal{L}(i_s) H(\hat{n}_i, \hat{n}_s) \mathcal{L}(i_i) S_v(\hat{n}_i) d\Omega + \frac{1}{4\pi} \int_{\Omega_*} \beta_d(\hat{n}_i) \mathcal{L}(i_s) H(\hat{n}_i, \hat{n}_s) \mathcal{L}(i_i) \mathbf{I}_*(\hat{n}_i) d\Omega \quad (7)$$

(see Jeffery 1989, 1990), where $\mathcal{L}(\gamma)$ is the 4×4 Mueller rotation matrix through angle γ , H is the 4×4 Hanle scattering phase matrix, \hat{n}_i and \hat{n}_s are unit vectors in the directions of the incident and scattered beams, and \mathbf{I}_* is the Stokes 4-vector for the intensity from the star. The angles i_s and i_i are the rotation angles that transform the Q_v and U_v components of the intensity vector from one set of coordinates to another. The coordinate systems for the star and observer are those described in INC. The directional escape probability is given by

$$\beta_d = \frac{1 - e^{-\tau_{\text{Sob}}(\hat{n})}}{\tau_{\text{Sob}}(\hat{n})}, \quad (8)$$

which is a function of direction \hat{n} through the optical depth dependence. Note that the first integral in equation (7) is over all angles, whereas the second for the incident stellar intensity is only over the solid angle Ω_* subtended by the star at the point of consideration.

The Sobolev optical depth in the line along the line of sight is given by

$$\tau_{\text{Sob}} = \int_{-\infty}^{\infty} \sigma_v n(r, \vartheta, \varphi) dZ, \quad (9)$$

where the line opacity σ_v is taken to be a δ -function in frequency, with $\sigma_v = \sigma_l \delta(v - v_Z)$, and v_Z is the frequency of the scattered light. However, v_Z is related to the velocity shift v_Z by $v_Z = v_{ul} + \Delta v_Z = v_{ul}(1 - v_Z/c)$. The δ -function representation for the line absorption, which is the fundamental approximation of Sobolev theory, ensures that the line optical depth, as integrated along a line of sight through the emitting envelope, is evaluated only at the isovelocity zone. Substituting for the δ -function, the Sobolev optical depth of equation (9) becomes

$$\tau_{\text{Sob}} = \int_{-\infty}^{\infty} \sigma_l n(r, \vartheta, \varphi) \delta(v - v_Z) dZ. \quad (10)$$

In the next section, this theory of line formation will provide the basis for our consideration of optically thin resonance-scattering lines.

3. OPTICALLY THIN LINE PROFILES WITH THE HANLE EFFECT

Although a sophisticated theory of polarized radiation transfer using the Hanle effect exists (Degl'Innocenti 1983; Stenflo 1994; Nagendra, Frisch, & Faurobert-Scholl 1999), it has been applied only to the Sun, especially to solar prominences (Bommier et al. 1994), turbulent solar magnetic fields (Stenflo 1982; Stenflo, Keller, & Gandorfer 1998), and the upper solar atmosphere (Bianda, Solanki, & Stenflo 1998). To explore applications of the Hanle effect for diagnosing magnetic fields of stars, we consider only lines with small Sobolev optical depths. We have simplified the calculations by ignoring stellar occultation and the continuum absorption by intervening wind material. We do not allow for any contribution to the line from the stellar photo-

sphere, nor do we account for the breakdown of the Sobolev approximation for line formation at the inner wind, where the flow speed is small.

Note that most of the effects being ignored will be of consequence only near line center. For example, we expect that the general effect of large line optical depths will be to isotropize the radiation field, leading to a reduction of the line polarization, and that the onset of high optical depths will occur first near line center, because the emission arises from the denser inner wind at these frequencies. In regard to contamination by photospheric absorption, a typical hot star may have a wind terminal speed of 1000–2000 km s⁻¹, a rotation speed of 100–300 km s⁻¹, and an isothermal sound speed of 10–20 km s⁻¹; hence only the central 10%–20% of the wind-broadened line profile will be modified by a photospheric contribution. Similarly, stellar occultation has the greatest consequence for the line emission occurring directly opposite to the observer from the star, which is typically a region of slow expansion. Continuum absorption by the stellar wind can have an effect over a significant range of line frequencies, but even then, only the shortward-shifted profile is modified (i.e., corresponding to outward-moving material between the observer and the star), whereas the longward-shifted part of the profile is not altered by the wind absorption. Outside the line core, the line emission will be optically thin, and Sobolev theory should be a good approximation to the line formation.

The optically thin limit requires that $\tau_{\text{Sob}}(v_Z) \lesssim 1$, in which case the intensity of equation (6) reduces to

$$\mathbf{I}_v \approx S_v \tau_{\text{Sob}}. \quad (11)$$

Substituting into equation (5) for the flux of scattered light yields

$$\mathcal{F}_{v,s} = \frac{1}{d^2} \int_{v_Z} S_v \tau_{\text{Sob}} dA. \quad (12)$$

To obtain the source function, we note that in the optically thin limit, $\beta_d \approx (1 - 1 + \tau_{\text{Sob}})/\tau_{\text{Sob}} = 1$, so that only the second integral over the stellar intensity field survives in equation (7). Treating the star as a point source for purposes of illuminating the scattering envelope, the source function for resonance-line scattering with the Hanle effect reduces to

$$S_v = \frac{\mathcal{F}_{v,*}}{4\pi} \mathbf{h}(r, \vartheta, \varphi) \quad (13)$$

(as shown by INC), where the flux from the star at radius r is $\mathcal{F}_{v,*} = L_{v,*}/4\pi r^2$, and $\mathbf{h} = (h_I, h_Q, h_U, h_V)$ is introduced here as a compact notation for the polarimetric properties of the scattered light. The vector \mathbf{h} is

$$\mathbf{h} = \mathcal{L}(i_s) H(\hat{n}_i, \hat{n}_s) \mathcal{L}(i_i) \hat{\mathbf{I}}_i, \quad (14)$$

where $\hat{\mathbf{I}}_i$ is the Stokes 4-vector for the incident intensity as normalized to the scalar stellar intensity I_* . The incident intensity is taken as unpolarized, so $\hat{\mathbf{I}}_i = (1, 0, 0, 0)$.

Substituting equation (13) for the source function and equation (9) for τ_{Sob} gives

$$\mathcal{F}_{v,s} = \frac{1}{d^2} \int_{v_Z} \left(\frac{\mathcal{F}_{v,*}}{4\pi} \mathbf{h} \right) [\sigma_l n \delta(v - v_Z) dZ] dA, \quad (15)$$

$$= \frac{\sigma_l L_{v,*}}{16\pi^2 d^2} \int_{v_Z} \frac{n}{r^2} \delta(v - v_Z) \mathbf{h} dV, \quad (16)$$

where the differential volume element $dV = dA dZ$. The single integral signifies a triple integral over the isovelocity zone. In the optically thin limit, stellar photons emerge from the envelope either directly or having scattered no more than once; hence the observed flux of scattered radiation reduces to a volume integration. Note that the volume integral may be evaluated in any set of coordinates, of which the most convenient are those of the star, because both the density and the magnetic field are most easily specified in that system.

3.1. Analytic Results for Planar Equatorial Disks

We derive the polarized line profiles for the case of an axisymmetric planar equatorial disk. The disk is assumed to expand radially with constant speed v_∞ . The line profiles resulting from this geometry have been considered by Wood & Brown (1994) and by Ignace (1998b) for the non-magnetic case, so the following derivations are extensions of theirs to the Hanle diagnostic problem.

Figure 4 shows an equatorial disk viewed at an inclination i from the observer's line of sight. The Z_* -axis is the symmetry axis of the disk. A point in the disk has cylindrical coordinates $(R, \varphi, 0)$. For a disk expanding at constant speed, the Doppler shift is derived from

$$v_z = -v_\infty \sin i \cos \varphi. \quad (17)$$

Since i and v_z are constant, the isovelocity zones reduce to a pair of radial "spokes" located at angles $\pm \varphi_0$ (see Fig. 4).

The flux arising from these two spokes is computed from equation (16). For a planar disk, it is the surface number density Σ that is of interest, which is determined by

$$\Sigma(R) = \int_{-\infty}^{+\infty} n dZ_* = \frac{\dot{M}}{2\pi\mu m_H R v_\infty}, \quad (18)$$

where μ is the mean molecular weight. Taking the differential volume element of equation (16) for the line flux to be $dV = R dR d\varphi dZ_*$, the observed flux is

$$\mathcal{F}_{v,s} = \frac{\sigma_l L_{v,*}}{16\pi^2 d^2} \int_{v_z} \frac{\Sigma(R)}{R^2} \delta(v - v_z) h(R, \varphi) R dR d\varphi. \quad (19)$$

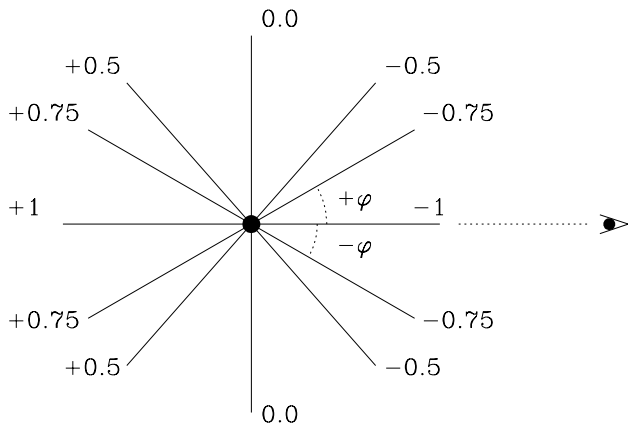


FIG. 4.—Locus of points in a radially expanding equatorial disk with constant velocity shift v_z . The isovelocity zones are radial "spokes" located symmetrically about the line of sight at $\pm \varphi$. The numbers appearing next to various spokes indicate the observed velocity shift, $v_z/(v_\infty \sin i)$, with positive for redshift and negative for blueshift.

The δ -function can be eliminated by employing the following property:

$$\int_0^\pi \delta[v - v_z(\varphi)] d\varphi = \frac{1}{|dv_z/d\varphi|_{\varphi_0}} \quad (20)$$

(as in Wood & Brown 1994), where by equation (17), φ_0 refers to the two radial spokes that have the velocity shift of interest. Because there are two spokes, the integral in φ is in the interval of 0 to π , instead of 0 to 2π . Manipulating equations (3) and (17) yields

$$\left| \frac{dv_z}{d\varphi} \right|_{\varphi_0} = \frac{1}{\lambda_{ul}} \left| \frac{dv_z}{d\varphi} \right|_{\varphi_0} = \frac{v_\infty \sin i}{\lambda_{ul}} |\sin \varphi_0|. \quad (21)$$

Combining equations (20) and (21) with equation (19) for the scattered flux gives

$$\mathcal{F}_{v,s} = \frac{\sigma_l L_{v,*} \lambda_{ul}}{16\pi^2 d^2 v_\infty \sin i} \int_{v_z} \frac{\Sigma(R)}{R |\sin \varphi_0|} h(R, \varphi_0) dR. \quad (22)$$

Using normalized variables with $x = R/R_*$ and taking $\Sigma = \Sigma_0/x$ from considerations of mass continuity, equation (22) can be rewritten as

$$\mathcal{F}_{v,s}(v_z) = \tau_0 \mathcal{F}_{v,0} \int_{v_z} \frac{h(x, \varphi_0)}{x^2 |\sin \varphi_0|} dx, \quad (23)$$

where the various constants are collected into the parameters

$$\mathcal{F}_{v,0} = \frac{L_{v,*}}{4\pi d^2}, \quad (24)$$

which is the direct stellar light, and

$$\tau_0 = \frac{\sigma_l \Sigma_0 \lambda_{ul}}{4\pi v_\infty \sin i}, \quad (25)$$

which is an optical depth scale parameter.

Even with the simplifying assumptions of a point-source star, an optically thin radiative transfer, and a thin equatorial disk, the ratio $h/|\sin \varphi|$ still poses a problem for the analytic evaluation of equation (23). There are, however, a few special cases that do yield analytic results that are worth deriving before proceeding to numerical evaluations. These cases include radial magnetic fields, B_r , axial magnetic fields, B_z , and toroidal magnetic fields, B_ϕ . The first case of B_r is trivial: there is no Hanle effect for magnetic fields that are symmetrically oriented with respect to the incident radiation field, which is the case for B_r given our assumption of a uniformly illuminated star. (In fact, even with limb darkening there will be no Hanle effect for $B = B_r$.) Consequently, the line polarization is unchanged by the Hanle effect. The other two cases of axial and toroidal fields are more interesting, and the polarized line profiles as altered by these fields are discussed in the next two sections.

3.1.1. The Case of an Axial Magnetic Field

An axial magnetic field is one that is oriented in the Z_* -direction, so the field lines are normal to the equatorial disk. Several geometrical simplifications result for this case: the incident stellar intensity is at right angles to the magnetic field, and the magnetic field direction is invariant to azimuthal position in the disk. As a result, the elements of the Hanle phase scattering vector \mathbf{h} (from INC) reduce to

$$h_I(R, \varphi, k_B) = 1 + \frac{1}{8}E_1(1 - 3 \cos^2 i) + \frac{3}{8}E_1 C(R, \varphi, k_B) \sin^2 i, \quad (26)$$

$$h_Q(R, \varphi, k_B) = \frac{3}{8}E_1 [\sin^2 i - C(R, \varphi, k_B)(1 + \cos^2 i)], \quad (27)$$

$$h_U(R, \varphi, k_B) = -\frac{3}{4}E_1 D(R, \varphi, k_B) \cos i, \quad (28)$$

$$h_V(R, \varphi, k_B) = 0. \quad (29)$$

The geometry is oriented so that a positive Q_v value corresponds to a polarization perpendicular to the disk, and a negative Q_v value to a polarization that is perpendicular to the Z_* -axis. The functions C and D are for this case:

$$C(R, \varphi, k_B) = \cos^2 \alpha_2(R, k_B) \cos 2\varphi - \frac{1}{2} \sin 2\alpha_2(R, k_B) \sin 2\varphi, \quad (30)$$

$$D(R, \varphi, k_B) = -\cos^2 \alpha_2(R, k_B) \sin 2\varphi - \frac{1}{2} \sin 2\alpha_2(R, k_B) \cos 2\varphi, \quad (31)$$

with $\varphi = \pm \varphi_0$. The angular parameter α_2 , defined in equation (1), is a function of radius through the dependence on the magnetic field strength, because $\tan \alpha_2 \propto B(R)$. For a quantitative calculation we chose to model the line profiles with an axial field that decreases with radius as $B_z = B_* x^{-1}$.

For our parametrization of the radial dependence of B_z , we have

$$\tan \alpha_2 = k_B x^{-1}. \quad (32)$$

Note that the Hanle effect provides information on both the magnitude and the direction of the field when $\tan \alpha_2 \sim 1$; in the saturated limit of large $\tan \alpha_2$, the Hanle effect is still sensitive to the field orientation but provides only a lower limit to its strength. However, in the optically thin limit that we are considering, the line polarization is strongly biased toward regions where the density of scatterers is greatest, which for an expanding wind with an assumed constant ionization fraction will be the innermost region. Consequently, the Hanle diagnostic will primarily be sensitive to the magnetic field at the inner wind. Since different lines will have different values for k_B , it will be important to obtain multiline spectropolarimetry to determine the field properties (a topic discussed at more length in § 3.2).

Substituting the Hanle vector \mathbf{h} for an axial magnetic field, using the parameter k_B , and integrating, the Stokes flux of equation (23) for the scattered light is found to be

$$\begin{aligned} \mathcal{F}_{I,s} &= \frac{3}{4} \tau_0 \mathcal{F}_{v,0} \\ &\times \left[\frac{8/3 + (1/3)E_1(1 - 3 \cos^2 i)}{\sin \varphi} + \frac{E_1 \sin^2 i \cos 2\varphi k_B^{-1} \tan^{-1} k_B}{\sin \varphi} \right], \quad (33) \end{aligned}$$

$$\begin{aligned} \mathcal{F}_{Q,s} &= \frac{3}{4} \tau_0 \mathcal{F}_{v,0} E_1 \\ &\times \left[\frac{\sin^2 i - (1 + \cos^2 i) \cos 2\varphi k_B^{-1} \tan^{-1} k_B}{\sin \varphi} \right], \quad (34) \end{aligned}$$

$$\mathcal{F}_{U,s} = \frac{3}{4} \tau_0 \mathcal{F}_{v,0} E_1 \left(\frac{\cos i \cos 2\varphi}{\sin \varphi} \right) k_B^{-1} \ln(1 + k_B^2), \quad (35)$$

$$\mathcal{F}_{V,s} = 0. \quad (36)$$

Note that the expressions for the flux of scattered light account for the *both* radial spokes at $\pm \varphi$; thus the angle φ appearing in equations (33)–(36) is in the interval from 0 to π . Note also that $\sin \varphi = (1 - v_z^2/v_{\max}^2)^{1/2}$ with $v_{\max} = v_0 \sin i$, so the I_v , Q_v , and U_v profiles tend to be “double horned,” with peak emission at $v_z/v_{\max} = \pm 1$. This type of profile shape is expected from a thin constant expansion disk (Struve 1931).

For pure dipole scattering with $E_1 = 1$, Figures 5 and 6 show the polarized line profiles as $\mathcal{F}_{Q,s}/\mathcal{F}_{I,s}$ and $\mathcal{F}_{U,s}/\mathcal{F}_{I,s}$ for several different viewing inclination angles with $i = 10^\circ$, 30° , 50° , 70° , and 90° and three different values of $k_B = B_*/B_{\text{Hanle}} = 0$ (solid lines), 2 (short-dashed lines), and 25 (long-dashed lines). We assume that there is negligible continuum polarization. The line emission near zero velocity shift arises from regions that are nearly orthogonal to the viewing line of sight. In contrast, emission in the line wings originates from material that is along the viewing line of sight, being forward scattered (near side) or backward scattered (far side). Consequently, the line polarization can be understood from matching the velocity shift to the scattering geometry.

As k_B increases from zero to larger values, the polarized line profile is affected in three ways: (1) the ratio $\mathcal{F}_{Q,s}/\mathcal{F}_{I,s}$ at small velocities becomes progressively smaller, (2) the ratio $\mathcal{F}_{Q,s}/\mathcal{F}_{I,s}$ becomes increasingly positive in the wings, and (3) the profile of $\mathcal{F}_{U,s}/\mathcal{F}_{I,s}$ is nonzero for intermediate values of k_B . These results can be understood from a consideration of the atomic oscillator model.

Consider the specific case of an edge-on disk with $i = 90^\circ$, in which case the U_v -polarization is identically zero. Recall that the components of an atomic oscillator that are parallel to the magnetic field will suffer no Hanle precession. The unpolarized light from the star consists of two electric field vectors, \mathcal{E}_\perp and \mathcal{E}_\parallel , that are mutually orthogonal and perpendicular to the radius vector. The component \mathcal{E}_\perp is taken

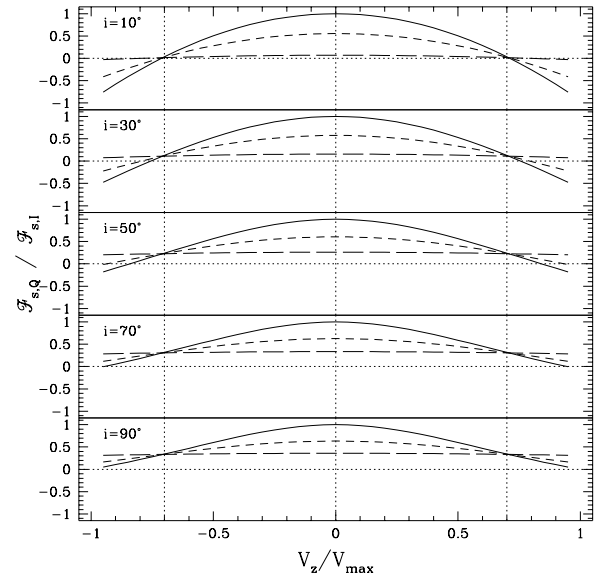


FIG. 5.—Line polarization $\mathcal{F}_{Q,s}/\mathcal{F}_{I,s}$ for an equatorial disk with an axial magnetic field, B_z , that is viewed at a sequence of inclination angles $i = 10^\circ$, 30° , 50° , 70° , and 90° . At each inclination the line polarization has been computed for three values of $k_B = 0$ (solid lines), 2 (short-dashed lines), and 25 (long-dashed lines). The sign indicates the position angle of the net polarization, with positive for polarization aligned with the Z_* -axis and negative for polarization perpendicular to the axis.

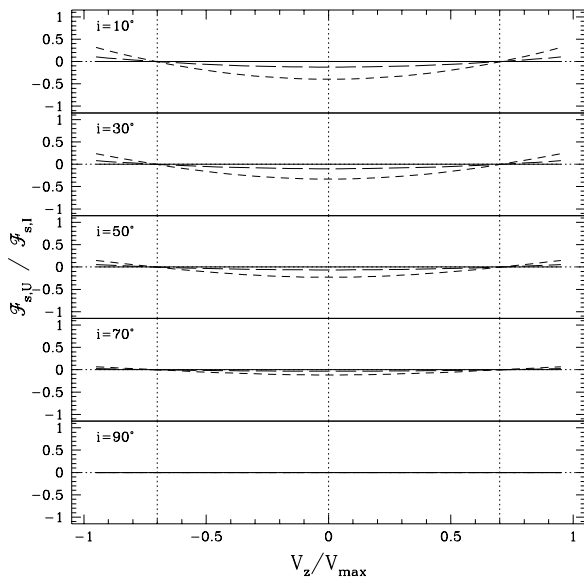


FIG. 6.—Polarized line profiles for an equatorial disk and magnetic field B_z , but now for $\mathcal{F}_{U,s}/\mathcal{F}_{I,s}$. As in Fig. 5, the inclination angles are indicated. The line types are also the same. Owing to axisymmetry, $\mathcal{F}_{U,s}$ is exactly zero in the absence of magnetic fields. The $\mathcal{F}_{U,s}$ flux is largest for disks viewed near pole-on yet tends to zero in the saturated limit of large k_B .

perpendicular to the equatorial plane, whereas \mathcal{E}_{\parallel} lies in the plane. For a magnetic field B_z , the Hanle precession is induced only on \mathcal{E}_{\parallel} . The Hanle effect causes this part of the oscillator to precess about the Z_* -direction, and the observer sees not just I_{\perp} but also a nonzero contribution from I_{\parallel} ; hence there is a depolarization relative to the zero field case at velocity shifts near line center.

The opposite effect occurs for forward and backward scattering. Normally, I_{\perp} and I_{\parallel} are observed in equal amounts for this scattering geometry. However, the Hanle precession causes part of I_{\parallel} to be scattered into other directions, thereby reducing the amount that is forward (backward) scattered. In this way a net polarization is actually produced at large velocity shifts. Note, however, that for an axial magnetic field, INC showed that the polarization integrated over the line does not depend on k_B .

In the limit of saturation, $k_B = B_*/B_{\text{Hanle}}$ becomes large, and the terms in which k_B appears in equations (33)–(36) tend toward zero. The profile for $\mathcal{F}_{Q,s}/\mathcal{F}_{I,s}$ approaches a constant value of $3E_1 \sin^2 i / [8 + E_1(1 - 3 \cos^2 i)]$; hence the line profile polarization is flat-topped. In contrast, that for $\mathcal{F}_{U,s}/\mathcal{F}_{I,s}$ is zero at all velocity shifts. This result can also be explained by the classical oscillator model. The magnetic field is everywhere normal to the disk. In the saturated limit, the polarization arising from any one scatterer in the disk is the same as that of any other. Although the flux of scattered light $\mathcal{F}_{I,s}$ and the flux of polarized light $\mathcal{F}_{Q,s}$ vary from one isovelocity zone to the next, they are proportional so that the ratio is constant. It is evident that the greatest deviation of the line polarization from the zero field case occurs for saturation where $k_B \gg 1$.

At this point it is worth interjecting a note about our convention for the line polarization. We define the total polarization of the line at velocity shift v_z to be $p(v_z) = (\mathcal{F}_{Q,s}^2 + \mathcal{F}_{U,s}^2)^{1/2} / \mathcal{F}_{I,s}$, which is the ratio of polarized light to total scattered light. This definition seems the natural representation for interpreting the scattering physics.

However, it is the practice of observers to measure the polarization as $p(v_z) = (\mathcal{F}_{Q,s}^2 + \mathcal{F}_{U,s}^2)^{1/2} / (\mathcal{F}_{I,s} + \mathcal{F}_{v,*})$, which is the ratio of total polarized flux to total observed flux, including both the scattered light and the direct stellar contribution. For optically thin line emission, $\mathcal{F}_{v,*}$ will typically exceed $\mathcal{F}_{I,s}$ by significant factors. The polarimetric convention typically adopted by observers is roughly obtained by multiplying our results by the factor $\mathcal{F}_{I,s}/\mathcal{F}_{v,*}$. In § 3.2, a numerical simulation of a dipole field in a spherically accelerating wind is presented where the conventional definition is adopted.

3.1.2. The Case of a Toroidal Magnetic Field

This section describes results for the formation of polarized line profiles in the case of a toroidal magnetic field. The toroidal field B_{ϕ} is perpendicular to the Z_* -axis; hence the orientation of B_{ϕ} relative to the observer now depends on azimuth ϕ . The derivation of the line polarization is somewhat lengthy and has therefore been relegated to the Appendix. Here we proceed to discuss the results of the derivations, for which polarized line profiles have been plotted in Figure 7.

The response of the line polarization to increasing values of k_B in the case of B_{ϕ} differs markedly from the case of B_z . Figure 3 shows that the polarization near line center decreases, but in the wings the modification of the polarization is more complicated, as evidenced by the appearance of asymmetries about line center. Note that unlike the case of axial fields, the polarized profile does not become flat-topped at large values of k_B . Moreover, at high inclination and large k_B values, nearly the whole profile changes sign, signifying a change of 90° rotation in the net polarization position angle. It is also to be noted that unlike the axial field case, $\mathcal{F}_{U,s}/\mathcal{F}_{I,s}$ is zero across the profile for all inclinations and field strengths (see Appendix).

To interpret the line profile results, consider again the atomic oscillator model. In the case of toroidal fields, B_{ϕ} is

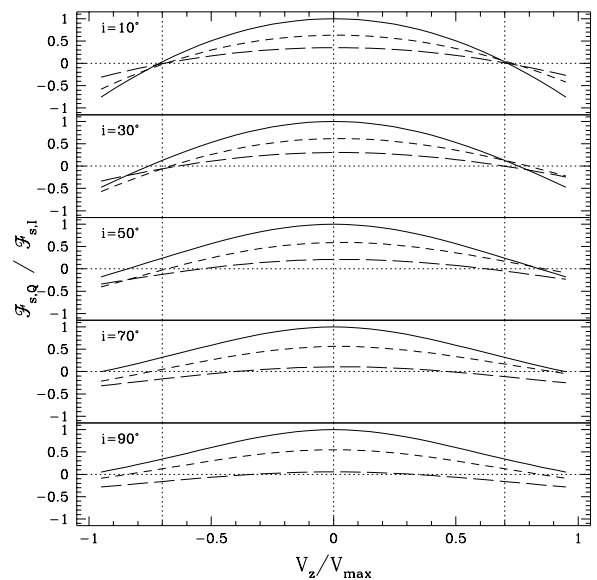


FIG. 7.—Polarized line profiles for an equatorial disk with a toroidal magnetic field, B_{ϕ} . In this case $\mathcal{F}_{U,s}$ vanishes identically at each point in the profile for all viewing inclinations; hence $\mathcal{F}_{Q,s}/\mathcal{F}_{I,s}$ is in fact the total line polarization. The profiles are computed with the same values of k_B as in Fig. 5. Note the presence of asymmetries about line center in the cases that $i \neq 90^\circ$. An explanation for these asymmetries is detailed in the text.

parallel to I_{\parallel} (instead of I_{\perp} , as was the case for B_Z). At zero velocity shift, the toroidal field is parallel to the observer's line of sight. Since B_{ϕ} and \mathcal{E}_{\parallel} are colinear, the \mathcal{E}_{\parallel} component of the oscillator is not Hanle precessed. However, \mathcal{E}_{\perp} does undergo precession, and the precession is about the line of sight; hence a net depolarization of the scattered starlight is observed.

At the velocity shifts of the wings, the toroidal field is perpendicular to the line of sight at the near and far sides of the scattering volume. Forward and backward scattering normally yield zero polarization, but the toroidal field causes \mathcal{E}_{\perp} to undergo precession. Hence I_{\perp} is reduced, and I_{\parallel} is left unchanged. The net polarization that results is oriented perpendicular to the symmetry axis of the disk, and by our convention the polarization is negative.

Unlike the case of B_Z , INC showed that the line-integrated polarization does *not* remain constant in the toroidal field case. As k_B is made to increase, the net line polarization is reduced, passes through zero at a critical field strength, and eventually becomes negative, which is completely consistent with the detailed profile analysis derived above.

Another important effect observed in the B_{ϕ} case that was not seen for B_Z is the appearance of line asymmetries. Using the atomic oscillator picture, the asymmetries arise from the fact that the toroidal field changes its orientation relative to the line of sight with azimuth around the disk. For example, a point on the near side of the star has B_{ϕ} along $+\phi$, whereas on the far side the field is directed along $-\phi$. Recall that the Hanle precession is in the direction of $-\mathbf{v} \times \mathbf{B}$ (negative owing to the electron charge); hence an observer viewing the scattering arising from the near side will see \mathcal{E}_{\perp} precessed toward them, but on the far side, the precession of \mathcal{E}_{\perp} is in the opposite sense, away from the observer. So, although the velocity field, and hence the scattering geometry, is back-front symmetric, the line polarization is not, because the fields at opposite points of the star are oppositely directed.

There are five main points that summarize the properties of the line asymmetries:

1. The line polarization coming from the near and far sides of the star are not the same. Figure 3 shows that the *magnitude* of the polarization in the blueshifted wings is greater than that in the redshifted wings.

2. The asymmetry becomes less apparent at large values of k_B because the saturation limit is reached. When saturated, the Hanle precession is so rapid that differences between the near (blueshifted) and far (redshifted) sides lose their distinction.

3. The asymmetry is less toward zero velocity shifts because, although B_{ϕ} on the right and left sides of the star point in opposite directions, the precession of \mathcal{E}_{\perp} is neither more toward nor more away from the observer. Thus no asymmetry in the line polarization can result.

4. The asymmetry is not observed for inclinations of $i = 0^{\circ}$ or 90° owing to the particular symmetry of these viewing perspectives. The Hanle precession of \mathcal{E}_{\perp} toward the observer on the near side and away from the observer on the far side cannot be distinguished.

5. Last, the results of Figure 3 are for $0^{\circ} < i < 90^{\circ}$ and B_{ϕ} in the $+\phi$ direction. If B_{ϕ} were in the $-\phi$ direction, the sense of the asymmetry would be reversed about line center. However, this same reversal is effected for B_{ϕ} in the $+\phi$

direction but viewing inclinations in the range $90^{\circ} < i < 180^{\circ}$ (i.e., for an observer who views the scattering from the opposite hemisphere). Hence, for an optically thin wind, there exists an ambiguity between the viewing inclination and the direction of B_{ϕ} .

3.2. Numerical Results for a Spherical Envelope

The advantage of having considered the thin-disk case is that the results are analytic, but the disadvantage is that applications are restricted to that particular geometry. We have therefore computed polarized line profiles for magnetized spherical envelopes as a consideration of a more realistic wind geometry. In the absence of a magnetic field, the line profiles have net zero polarization owing to the symmetric distribution of the scatterers. The addition of a magnetic field provides a global asymmetry of the system; hence the net line polarization isolates the effects of the magnetic fields. Outside the line frequencies, the continuum polarization from electron scattering remains zero.

We have made numerical calculations for an accelerating spherical wind with a dipole magnetic field. The combination of this wind geometry and magnetic topology allows us to explore the effects of a nonconstant wind flow for the polarized profile. Spherical symmetry ensures that the location of the isovelocity zones are independent of viewing inclination; however, the defining axis of the dipole field can be oblique to the line of sight, so that the magnetic field intercepts the isovelocity zones in a complicated way.

It is therefore worthwhile applying the results of the previous section in order to anticipate the trends from the numerical results in the dipole field case. The dipole field is purely axial in the equatorial plane, and the previous results derived for an axial field and a planar disk are relevant. In the vicinity of the polar latitudes (i.e., as defined by the axis of the dipole field), the magnetic field is nearly radial, exactly so on the axis, so that the line polarization remains largely unchanged by the Hanle effect for resonance scattering in that region.

Consider the two extreme viewing perspectives of pole-on and edge-on. The pole-on case is trivial since both the field distribution and the distribution of scatterers are axially symmetric; hence the polarization is zero throughout the line profile owing to the polarimetric cancellation. The edge-on case is more interesting. Retaining the assumption of a constant velocity flow for purposes of discussion, the extreme blueshifted line emission arises along the line of sight on the near side of the star, where the dipole field is everywhere axial. The wing emission should therefore be unpolarized in the absence of a field but should become increasingly polarized with increasing field strength. Ignoring occultation, the same polarimetric signature will be observed in the extreme redshifted wing. For both the extreme blue and red wings, the polarization position angle is parallel to the symmetry axis. Even in the case of an accelerating wind, the emission at the line wings should be most sensitive to the axial fields near the equatorial plane.

Near line center the situation is more complicated, because the line emission arises in the plane of the sky, and the intersection of the dipole field with that plane displays the full variation of the field orientation with latitude. Moreover, the field strength for a fixed radius also varies with latitude, being twice as strong at the pole than the

equator. However, as we have already noted, the dipole field is essentially radial near the pole and axial at the equator. So at line center the polarization is zero for $B_* = 0$, but as the field strength is increased, the polarized line emission is little affected by the field at high latitudes; only the fields from midlatitudes toward the equator are important for producing a Hanle effect. In the case of an accelerating wind, the line emission is dominated by resonance scattering from everywhere at the inner wind, where the flow speed is small compared with terminal. Hence the line scattering samples the full range of scattering geometries, and the line emission is strong owing to the higher density.

As an illustrative calculation, we have chosen to focus on ζ Ori O9.5 Ia, which has been intensely studied for stellar wind phenomena. The lack of polarization at visible wavelengths indicates that the wind of ζ Ori is not highly distorted. However, Cassinelli & Swank (1983) argued, from the presence of a 2.2 keV spectral feature obtained with the *Einstein* solid-state spectrometer, that the star has gas at about 20×10^6 K, suggesting confinement by field strengths of 20–100 G, which should be detected easily by the Hanle effect. Thus a spherical wind with a dipole field is the most reasonable first approximation to the geometry of this star.

The top panel of Figure 8 shows the *Copernicus* spectrum of ζ Ori, exhibiting a number of unsaturated (optically thin) P Cygni wind lines. In the simulation we assume that the star is observed equator-on as defined by the dipole field. The spherical wind is taken to have a terminal speed of 2500 km s^{-1} and a standard $\beta = 0.5$ velocity law. The abundance of the scattering ions is assumed uniform (not stratified). The Hanle effect line profiles are estimated for three multiplets, the S IV triplet at 1063, 1073, and 1074 Å, the N V doublet at 1239 and 1243 Å, and the Si IV doublet at 1394 and 1403 Å. A fourth P Cygni line seen in the spectrum, C III $\lambda 1175$, is a sextuplet from a metastable state. It will exhibit a Hanle effect but has not been modeled here because of the

spectroscopic complications. For each member of each modeled line, we assume that the wind consists of concentric spherical shells, and the total profile is a superposition of the emission arising from each shell (as in Cassinelli & MacGregor 1986), using shell averages given in INC.

Table 1 shows the spectroscopic data used for this calculation. The value of E_1 for each scattering process (excitation and de-excitation) is calculated using formulae given in Stenflo (1994), which depend on the total angular momentum of the initial state j_i , the intermediate state j_m , and the final state j_f . A negative E_1 corresponds to polarization in the plane of the scattering. This sometimes occurs for fluorescent scattering, where the initial state is not the same as the final. Most of the observed lines are resonance doublets, where each observed emission line corresponds to a unique scattering process. For the S IV multiplet, however, two of the three emission lines, $\lambda 1062.7$ and $\lambda 1073.5$, consist of superposed resonance and fluorescence lines. In the table the resonance member is listed first. These were combined by assuming that the relative strengths of the two lines is given by the statistical equilibrium population ratio of their initial states, giving an “effective” E_1 for S IV $\lambda 1062.7$ and $\lambda 1073.0$. The Hanle field sensitivity is also tabulated in the rightmost column.

To compute the net observed polarization we assume that an unpolarized stellar continuum underlies the polarized resonance lines. This continuum is taken to be flat, except in the P Cygni absorption, where it is reduced to 0.33, 0.2, and 0.17 of the continuum value for the S IV, N V, and Si IV lines, respectively. The continuum value is determined from the *Copernicus* spectrum at wavelengths just beyond the line absorption. It is assumed that the P Cygni absorption results purely from wind attenuation of the stellar continuum.

The line emission at each wavelength is taken from the Hanle effect calculation, with the three lines normalized to values of 0.33, 0.67, and 0.55 of the local continuum level at a velocity shift of $\Delta v/v_\infty = 0.2$. The polarization of the line emission at each wavelength is taken from the Hanle calculation for Doppler shift $|\Delta v/v_\infty| > 0.2$. In the line core, optical depth effects invalidate the intensity and polarization calculation, so we set the polarization to zero there, assuming that multiple scattering will completely isotropize

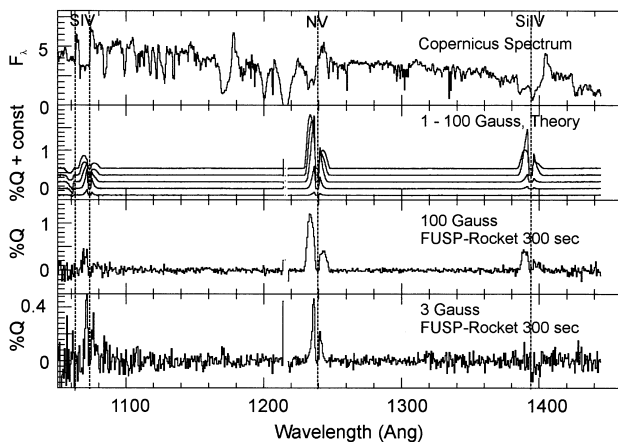


FIG. 8.—Numerical simulation of the Hanle effect for a dipole magnetic field in a spherical wind. The top panel shows a *Copernicus* spectrum of ζ Ori, with flux F_λ in units of $10^{-8} \text{ ergs s}^{-1} \text{ cm}^{-2} \text{ \AA}^{-1}$. The panel below shows theoretical polarized profiles evaluated at field strengths of 1, 3, 10, 30, and 100 G at the wind base. Note that the continuum polarization is zero, but a constant offset between the curves has been added to show the results better. The lower two panels simulate a 300 s FUSP exposure for magnetic field strengths of 100 and 3 G. The two major results are that (1) magnetic fields produce line polarization even in spherically symmetric flows, and (2) the response of different lines to the Hanle effect can be used to infer the field strength.

TABLE 1
FAR-ULTRAVIOLET RESONANCE LINES

Line	j_i	j_m	j_f	E_1	B_{Hanle} (G)
O VI $\lambda 1031.9$	1/2	3/2	1/2	0.5	17.8
O VI $\lambda 1037.6$	1/2	1/2	1/2	0.0	...
S IV $\lambda 1062.7$	1/2	3/2	1/2	0.5	8.3
	3/2	3/2	1/2	-0.4	...
S IV $\lambda 1073.0$	3/2	5/2	3/2	0.28	6.5
S IV $\lambda 1073.5$	3/2	3/2	3/2	0.32	1.6
	1/2	3/2	3/2	-0.4	...
P V $\lambda 1118.0$	1/2	3/2	1/2	0.5	53.9
P V $\lambda 1128.0$	1/2	1/2	1/2	0.0	...
N V $\lambda 1238.8$	1/2	3/2	1/2	0.5	14.6
N V $\lambda 1242.8$	1/2	1/2	1/2	0.0	...
Si IV $\lambda 1393.8$	1/2	3/2	1/2	0.5	37.7
Si IV $\lambda 1402.8$	1/2	3/2	1/2	0.0	...
C IV $\lambda 1548.2$	1/2	3/2	1/2	0.5	11.3
C IV $\lambda 1550.8$	1/2	1/2	1/2	0.0	...

the radiation field at these wavelengths in the line. These estimates for the P Cygni absorption, line flux, and line core width are based on the qualitative appearance of the *Copernicus* spectrum, taking into account the wind emission filling in the absorption and the photospheric depression of the continuum. The resulting systematic error in the polarization profile is no worse than a factor of 2.

The second panel in Figure 8 shows the theoretical polarization signature that we calculate as a function of wavelength for dipole strengths of 1, 3, 10, 30, and 100 G at the base of the wind. (The continuum polarization is zero in each case, but the polarized profiles are shifted up for clarity). Note that polarimetric effects set in for each line in the order of B_{Hanle} for that line (i.e., S IV, then N V, then Si IV). Note also that the polarized profile shapes change for a particular line, saturating successively farther out in the wings as k_B increases. If the inclination were different from 90° , there would also be a polarization position angle profile that is symmetric about line center. If the field were obliquely oriented relative to the rotation axis of the star, there would be a periodic change in the polarimetric features (e.g., periodicity in the X-ray flux of the O7 V star θ^1 Ori C, believed to be an oblique magnetic rotator, has been discovered by Gagné et al. 1997). The polarization and position angle profiles are different for different magnetic field geometries. Thus, not only can the field strength be estimated, but constraints can also be placed on the field configuration and inclination. This would be a *major* advance over our current state of knowledge.

To demonstrate that these effects are detectable in practice, we show in the bottom two panels of Figure 8 a simulated observation of ζ Ori made for a sounding rocket instrument currently in development, the Far-Ultraviolet Spectropolarimeter (hereafter FUSP; Nordsieck et al. 1994; Nordsieck 1999). FUSP will have an effective area of 57 cm^2 and a spectral resolution $\lambda/\Delta\lambda = 2000$ from 1050 to 1500 Å. Noise has been added appropriate to a 300 s FUSP observation, for base fields of 100 and 3 G. Note that the vertical scale has been increased in each for clarity. The simulation shows that a base field of 3 G (hence $B < 1$ G over most of the envelope) will be detectable; somewhat larger fields should easily be seen.

4. CONCLUSIONS

Model line profiles have been calculated for axial and toroidal magnetic fields in optically thin axisymmetric equatorial disks and for a dipole field in a spherical wind. The magnetic field can cause significant deviations of the polarized line profile from that obtained in the absence of magnetic fields, including flattening of the profile, position

angle flips, and asymmetries of the profile shape. The occurrence and degree of these effects depend on the magnetic geometry, the surface field strength, and the viewing perspective. In contrast to the integrated line polarizations discussed in INC, it is clear that more information about the magnetic field structure is available from well-resolved polarized lines. A given velocity shift in the line profile corresponds to a localized region of space in the wind, so the Hanle effect could be used to probe the magnetic field strength and orientation in each region separately.

To employ the Hanle diagnostic realistically, it will be crucial to exploit the fact that k_B depends on the A -value. Profile measurements of several lines should show systematic differences as a function of A_{ul} , as is demonstrated in the simulation of Figure 8. The comparison of different polarized lines can be used to infer the magnetic properties of the flow.

Observationally, the best possible case is to have several lines with a wide range of magnetic sensitivities to polarimetrically “map” the circumstellar field of unresolved envelopes. At the very least, it is desirable to have at least one line of large k_B and a second of small k_B . Lines in the saturated limit provide information about the magnetic field geometry, whereas the unaffected lines are useful for deriving the underlying geometry of scatterers. Although just two such lines are sufficient to place lower and upper limits on the surface field strength, a third line of intermediate sensitivity would be needed to measure it more definitively.

The results presented in this paper indicate that the Hanle effect is a potentially powerful diagnostic of modest stellar magnetic fields. There is an immense parameter space that remains to be investigated, and the interpretation of observational profile polarizations is likely to be more complicated than what we have considered. In future studies we plan to investigate finite star effects (e.g., occultation), radiative transfer effects of overlapping multiplet components and the consequences of optical depth effects, and periodicity associated with oblique magnetic fields. Also a more complete calculation should be made to properly account for P Cygni absorption and for realistic line broadening (e.g., as in the SEI method of Lamers, Cerruti-Sola, & Perinotto 1987).

R. I. wishes to acknowledge discussions with J. E. Bjorkman and K. Wood. The authors thank an anonymous referee for comments leading to improvements of this paper. This research was supported by NASA grant NAG5-2854 and a PPARC rolling grant.

APPENDIX

DERIVATION OF THE STOKES FLUX FOR THE CASE OF A TOROIDAL MAGNETIC FIELD

Here we present the derivation of the polarized profiles in the case of a toroidal magnetic field and a constant expansion equatorial disk. Figure 9 shows the scattering geometry. The intensity I_i is incident on the atom (located at the origin) with direction φ_i and $\mathcal{G}_i = \pi/2$. The toroidal field is located at $\mathcal{G}_B = \pi/2$ and $\varphi_B = \varphi_i + \pi/2$. The scattered intensity, $I_{v,s}$, is fixed at $\varphi_s = 0$ and directed toward the observer at inclination i .

To derive the Stokes flux vector components for the toroidal field case, we start by considering the components of \mathbf{h} :

$$h_I(R, \varphi, k_B) = H_{II}, \quad (\text{A1})$$

$$h_Q(R, \varphi, k_B) = H_{QI} \cos 2i_s + H_{UI} \sin 2i_s, \quad (\text{A2})$$

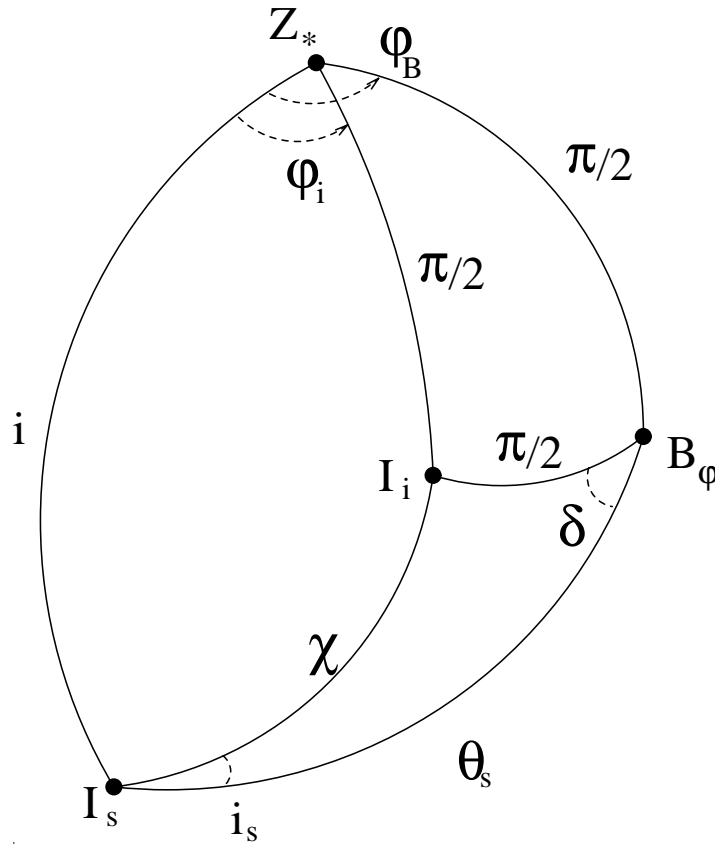


FIG. 9.—Spherical geometry associated with resonance-line scattering in an equatorial disk with a toroidal magnetic field. The scattering atom is located at the origin. The solid dots mark the end points of unit vectors for the disk symmetry axis Z_* , incident stellar intensity I_i , intensity scattered toward the observer I_s , and the toroidal magnetic field B_φ . The various angles are defined in text.

$$h_U(R, \varphi, k_B) = -H_{QI} \sin 2i_s + H_{UI} \cos 2i_s, \tag{A3}$$

$$h_V(R, \varphi, k_B) = 0, \tag{A4}$$

where i_s relates to φ through the following spherical trigonometric relations:

$$\cos 2i_s = \frac{\sin^2 \varphi \cos^2 i - \cos^2 \varphi}{1 - \cos^2 \theta_s}, \tag{A5}$$

$$\sin 2i_s = -\frac{\cos i \cos \varphi \sin \varphi}{1 - \cos^2 \theta_s}, \tag{A6}$$

where $\cos \theta_s = -\sin i \sin \varphi$. The H 's are elements of the 4×4 scattering phase matrix given in Appendix A of INC. For the geometry of interest, these matrix elements are

$$H_{II}(R, \varphi) = 1 + \frac{1}{8}E_1(1 - 3 \cos^2 \theta_s) + \frac{3}{8}C(R, \varphi, k_B)(1 - \cos^2 \theta_s), \tag{A7}$$

$$H_{QI}(R, \varphi) = \frac{3}{8}E_1[(1 - \cos^2 \theta_s) - C(R, \varphi, k_B)(1 + \cos^2 \theta_s)], \tag{A8}$$

$$H_{UI}(R, \varphi) = \frac{3}{4}E_1 D(R, \varphi, k_B) \cos \theta_s, \tag{A9}$$

$$H_{VI}(R, \varphi) = 0, \tag{A10}$$

where $\cos \theta_s = -\sin i \sin \varphi$. The functions C and D are

$$C(R, \varphi, k_B) = \cos^2 \alpha_2(R, k_B) \cos 2\delta - \frac{1}{2} \sin 2\alpha_2(R, k_B) \sin 2\delta, \tag{A11}$$

$$D(R, \varphi, k_B) = -\cos^2 \alpha_2(R, k_B) \sin 2\delta - \frac{1}{2} \sin 2\alpha_2(R, k_B) \cos 2\delta, \tag{A12}$$

where δ is related to the azimuth by

$$\cos 2\delta = \frac{\sin^2 i \cos^2 \varphi - \cos^2 i}{1 - \cos^2 \theta_s}, \tag{A13}$$

$$\sin 2\delta = 2 \frac{\cos i \sin i \cos \varphi}{1 - \cos^2 \theta_s}. \tag{A14}$$

Using equation (23) for the Stokes flux plus the relations given above, the components of the Stokes flux for the light scattered in just *one radial spoke* at $\pm \varphi$ become

$$\mathcal{F}_{I,s} = \frac{\tau_0 \mathcal{F}_{v,0}}{|\sin \varphi|} \left[1 + \frac{1}{8} E_1(1 - 3 \sin^2 i \sin^2 \varphi) + \frac{3}{8} E_1(\sin^2 i \cos^2 \varphi - \cos^2 i) k_B^{-1} \tan^{-1} k_B \right. \\ \left. + \frac{3}{16} E_1 \sin 2i \cos \varphi k_B^{-1} \ln(1 + k_B^2) \right], \quad (\text{A15})$$

$$\mathcal{F}_{Q,s} = \frac{3}{8} \frac{\tau_0 \mathcal{F}_{v,0}}{|\sin \varphi|} \left\{ \sin^2 \varphi \cos^2 i - \cos^2 \varphi + k_B^{-1} \tan^{-1} k_B [2 \sin 2i_s \sin 2\delta \cos \theta_s \right. \\ \left. - \cos 2i_s \cos 2\delta (1 - \cos^2 \theta_s)] - \frac{1}{2} k_B^{-1} \ln(1 + k_B^2) [2 \sin 2i_s \cos 2\delta \cos \theta_s + \cos 2i_s \sin 2\delta (1 + \cos^2 \theta_s)] \right\}, \quad (\text{A16})$$

$$\mathcal{F}_{U,s} = \frac{3}{8} \frac{\tau_0 \mathcal{F}_{v,0}}{|\sin \varphi|} \left\{ 2 \sin \varphi \cos \varphi \cos i + k_B^{-1} \tan^{-1} k_B [2 \sin 2i_s \cos 2\delta (1 + \cos^2 \theta_s) \right. \\ \left. + 2 \cos 2i_s \sin 2\delta \cos \theta_s] + \frac{1}{2} k_B^{-1} \ln(1 + k_B^2) [\sin 2i_s \sin 2\delta (1 + \cos^2 \theta_s) - 2 \cos 2i_s \cos 2\delta \cos \theta_s] \right\}, \quad (\text{A17})$$

$$\mathcal{F}_{V,s} = 0. \quad (\text{A18})$$

Note that in equations (A15)–(A18) we have not substituted for the angles ϑ_s , i_s , or δ , since the expressions would become unwieldy. Inspection of the various terms in the expressions reveals that each one for $\mathcal{F}_{I,s}$ and $\mathcal{F}_{Q,s}$ is even in azimuth, whereas those for $\mathcal{F}_{U,s}$ are odd. The total Stokes flux of scattered light from both radial spokes will thus increase $\mathcal{F}_{I,s}$ and $\mathcal{F}_{Q,s}$ in equations (A15) and (A16) by a factor of 2, but $\mathcal{F}_{U,s}$ will reduce identically to zero. As a result, there is no net U_v flux from a toroidal field in an axisymmetric equatorial disk.

REFERENCES

- Babcock, H. W. 1958, *ApJS*, 3, 141
 Biana, M., Solanki, S. K., & Stenflo, J. O. 1998, *A&A*, 331, 760
 Biermann, P. L., & Cassinelli, J. P. 1993, *A&A*, 277, 691
 Bommier, V., Degl Innocenti, E. L., Leroy, J.-L., & Sahal-Br  chet, S. 1994, *Sol. Phys.*, 152, 231
 Borra, E. F., & Landsteet, J. D. 1980, *ApJS*, 42, 421
 Brandt, J. C. 1970, *Introduction to the Solar Wind* (San Francisco: W. H. Freeman)
 Carter, B., Brown, S., Donati, J.-F., Rees, D., & Semel, M. 1996, *Publ. Astron. Soc. Australia*, 13, 150
 Cassinelli, J. P. 1998, in *Cyclical Variability in Stellar Winds*, ed. L. Kaper & A. W. Fullerton (Berlin: Springer), 237
 Cassinelli, J. P. & MacGregor, K. B. 1986, in *Physics of the Sun*, Vol. 3, ed. P. A. Sturrock (Dordrecht: Reidel), 47
 Cassinelli, J. P., & Swank, J. H. 1983, *ApJ*, 271, 681
 Chandrasekhar, S. 1960, *Radiative Transfer* (New York: Dover)
 Chen, W., & White, R. L. 1991, *ApJ*, 366, 512
 Collins, G. W., II. 1989, *The Fundamentals of Stellar Astrophysics* (New York: Freeman)
 Degl Innocenti, E. 1983, *Sol. Phys.*, 83, 3
 Donati, J.-F., Semel, M., Carter, B. D., Rees, D. E., & Cameron, A. C. 1997, *MNRAS*, 291, 658
 Elridge, J. A. 1924, *Phys. Rev.*, 24, 234
 Friend, D. B., & MacGregor, K. B. 1984, *ApJ*, 282, 591
 Gagn  , M., Caillault, J.-P., Stauffer, J. R., & Linsky, J. L. 1997, *ApJ*, 478, L87
 Gilliland, R. L., & Dupree, A. K. 1996, *ApJ*, 463, 29
 Hamilton, D. R. 1947, *ApJ*, 106, 457
 Hanle, W. 1924, *Z. Phys.*, 30, 93
 Ignace, R. 1998a, *A&A*, 332, 686
 ———. 1998b, *A&A*, 337, 819
 Ignace, R., Cassinelli, J. P., & Bjorkman, J. E. 1998, *ApJ*, 505, 910
 Ignace, R., Nordsieck, K. H., & Cassinelli, J. P. 1997, *ApJ*, 486, 550
 Jeffery, D. J. 1989, *ApJS*, 71, 951
 ———. 1990, *ApJ*, 352, 267
 Lamers, H. J. G. L. M., Cerruti-Sola, & Perinotto. 1987, *ApJ*, 314, 726
 Mathys, G. 1991, *A&AS*, 89, 121
 McLean, I. S. 1979, *MNRAS*, 186, 265
 Mihalas, D. 1978, *Stellar Atmospheres* (New York: Freeman)
 Moruzzi, G., & Strumia, F., eds. 1991, *The Hanle Effect and Level-Crossing Spectroscopy* (New York: Plenum)
 Nagendra, K. N., Frisch, H., & Faurobert-Scholl, M. 1999, *A&A*, 332, 610
 Nordsieck, K. H. 1999, in *ASP Conf. Ser. 164, Ultraviolet-Optical Space Astronomy Beyond HST*, ed. J. A. Morse, J. M. Schull, & A. L. Kinney (San Francisco: ASP), in press
 Nordsieck, K. H., Marcum, P., Jaehnig, K. P., & Michalski, D. E. 1994, *Proc. SPIE*, 2010, 28
 Parker, E. N. 1958, *ApJ*, 128, 664
 Poe, C. H., & Friend, D. B. 1986, *ApJ*, 311, 317
 Poekert, R., & Marlborough, J. M. 1978, *ApJ*, 220, 940
 Shore, S. N., & Brown, D. N. 1990, *ApJ*, 365, 655
 Shore, S. N., Brown, D. N., Sonneborn, G., Landstreet, J. D., & Bohlender, D. A. 1990, *ApJ*, 348, 242
 Sobolev, V. 1957, *Soviet Astron.*, 1, 678
 ———. 1960, *Moving Envelopes of Stars* (Cambridge: Harvard Univ. Press)
 Stenflo, J. O. 1982, *Sol. Phys.*, 32, 41
 ———. 1994, *Solar Magnetic Fields* (Dordrecht: Kluwer)
 Stenflo, J. O., Keller, C. U., & Gandorfer, A. 1998, *A&A*, 329, 319
 Stenflo, J. O., & Nagendra, K. N., eds. 1996, *Sol. Phys.*, 164(1–2)
 Struve, O. 1931, *ApJ*, 73, 94
 Wood, K., & Brown, J. C. 1994, *A&A*, 285, 220
 Wood, K., Brown, J. C., & Fox, G. K. 1993, *A&A*, 271, 492